Supporting Information

Monovalent Sulfur Oxoanions Enable Millimeter-Long Single Crystalline *h*-WO_3 Nanowire Synthesis

Guozhu Zhang,[1] Chen Wang,[1] Wataru Mizukami,[2] Takuro Hosomi,[1] Kazuki Nagashima,[1] Hideto Yoshida,[3] Kentaro Nakamura,[1] Tsunaki Takahashi,[1] Masaki Kanai,[1] Takao Yasui,[4] Yuriko Aoki,[2] Yoshinobu Baba[4] and Takeshi Yanagida[1,2]*

[1] Institute for Materials Chemistry and Engineering, Kyushu University, 6-1 Kasuga-Koen, Kasuga, Fukuoka, 816-8580, Japan

[2] Interdisciplinary Graduate School of Engineering Sciences, Kyushu University, 6-1 Kasuga-Koen, Kasuga, Fukuoka, 816-8580, Japan

[3] The Institute of Scientific and Industrial Research, Osaka University, 8-1 Mihogaoka, Ibaraki, Osaka 567-0047 Japan

[4]Graduate School of Engineering, Nagoya University, Furo-cho, Chikusa-ku, Nagoya 464-8603, Japan

Part I *h*-WO_3 nanowire growth

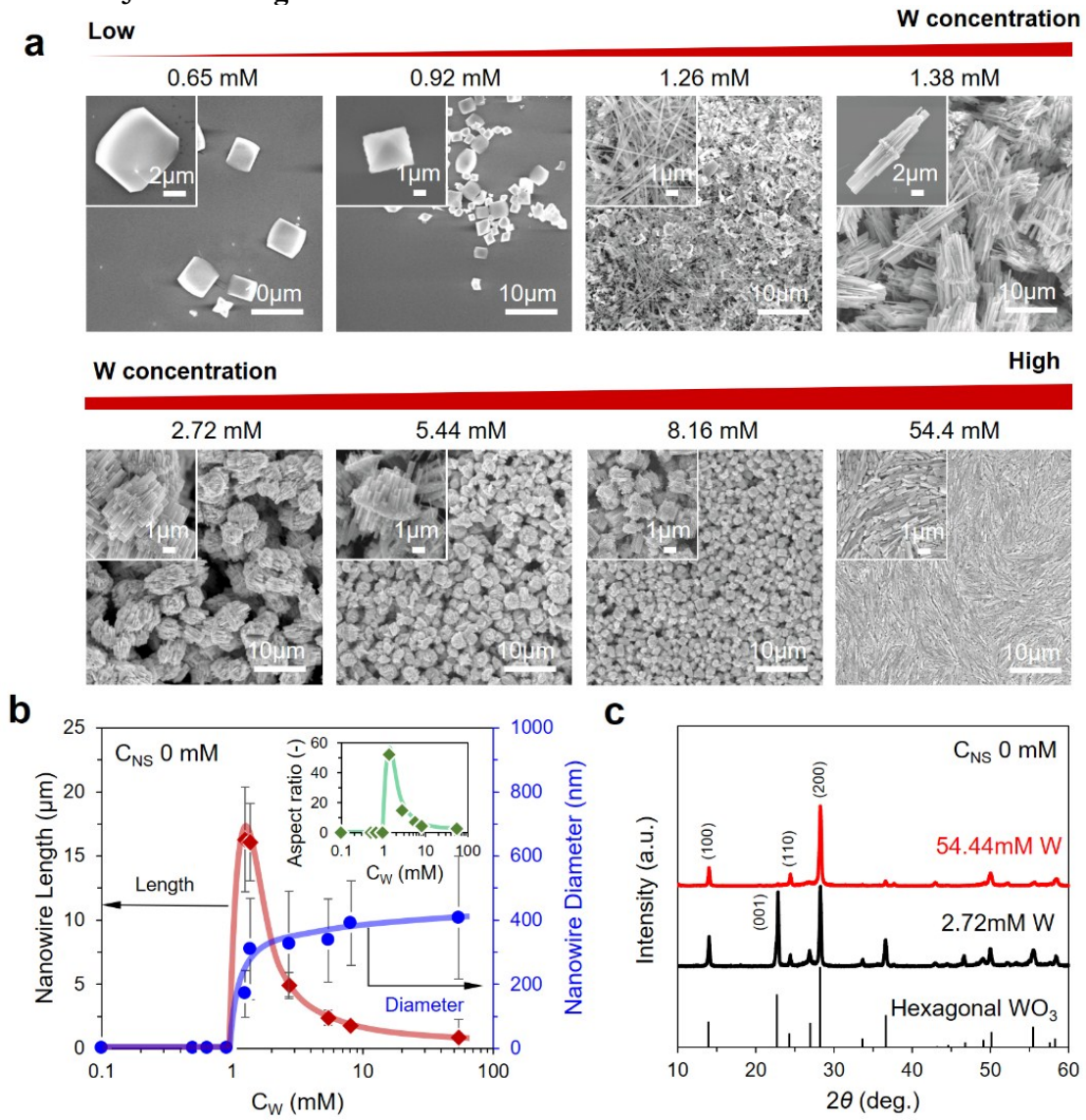

Figure S1. Effect of tungsten precursor concentration (C_W) on h-WO_3 nanowire morphologies (Without Na_2SO_4) when varying concentration of tungsten precursor from 0.65 to 54.4 mM. All growth experiments are performed at 200°C for 24 h, initial pH 1.68. (a) SEM images of nanowires grown without Na_2SO_4; (b) Tungsten precursor concentration dependence on the nanowire morphology data (including length and radius, from (a)) and the aspect ratio (insert); (c) XRD patterns of *h*-WO_3 nanowires grown with different concentration of tungsten precursor.

For the tungsten precursor concentration lower than 1.26 mM, there is no visible crystal growth due to the diluted environment. Above 1.26 mM, the nanowires start to grow. However, with the further increase of C_W above 1.38 mM, the nanowires tend to grow even along lateral direction, resulting in an increase in nanowire diameter and a decrease in length.

The aspect ratio data shows the maximum between 1.26 and 1.38 mM, highlighting the significant role of tungsten precursor concentration on the nanowire growth rate.

Here we discuss what essentially causes the concentration dependence on the nanowire growth rate and direction. As the C_W is low, the decomposition rate of precursor is extremely slow and the homogeneous nucleation process will be suppressed. Instead, the precursor atoms will preferentially nucleate on the crystal plane that with high surface free energy (Crystal growth for beginner, World scientific, Singapore, 1995). In the case of hexagonal WO_3 crystal, the axial (001) polar planes have a higher surface energy (0.09 eV/Å^2) as compared with side (100) planes, 0.04 eV/Å^2 (J. Mater. Chem. A, 2016, 4,11498). Thus, as the C_W lower than 1.26 mM, nucleation only emerges at (001) planes and growth of other crystal planes are almost suppressed. With the C_W further increase from 1.38 mM to 54.4 mM, nucleation at (100) plane also will start. In addition, high concentration of precursor would cause homogenously growth of WO_3 nuclei in the bulk solution. As a result, the anisotropic crystal growth along ⟨001⟩ no longer exists and the crystal growth along lateral directions can coexist. Therefore, the variation of concentration seems to affect not only the nucleation process but also the growth rate.

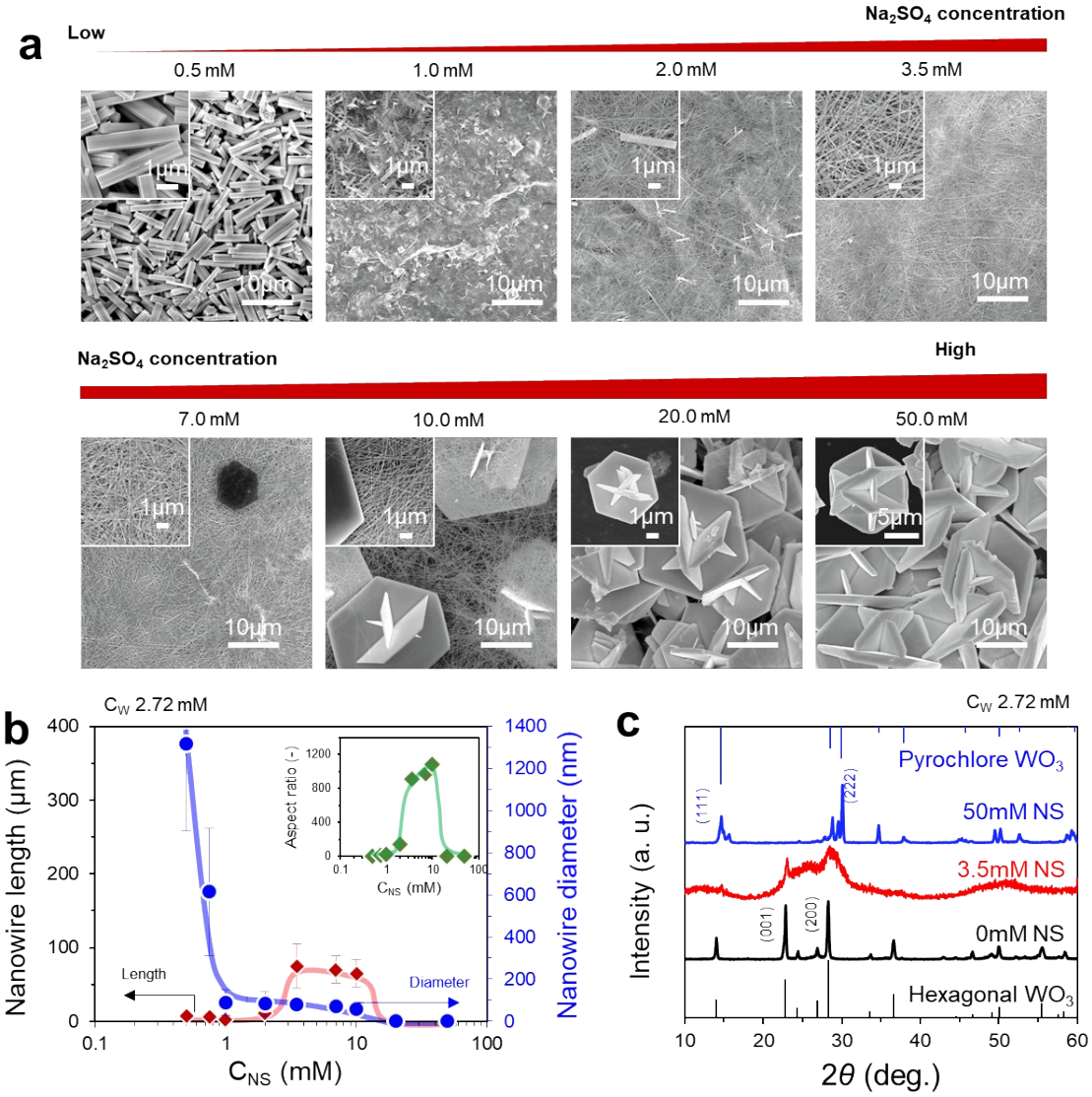

Figure S2. Effect of Na_2SO_4 concentration (C_{NS}) on *h*-WO_3 nanowire morphologies (2.72mM tungsten precursor) when varying concentration of Na_2SO_4 from 0.5 to 50mM. All growth experiments are performed at 200°C for 24 h, initial pH 1.68. (a) SEM images of nanowires grown with 2.72mM tungsten precursor; (b) Tungsten precursor concentration dependence on the nanowire morphology data (including length and radius, from (a)) and the aspect ratio (insert); (c) XRD patterns of *h*-WO_3 nanowires grown with different concentration of Na_2SO_4.

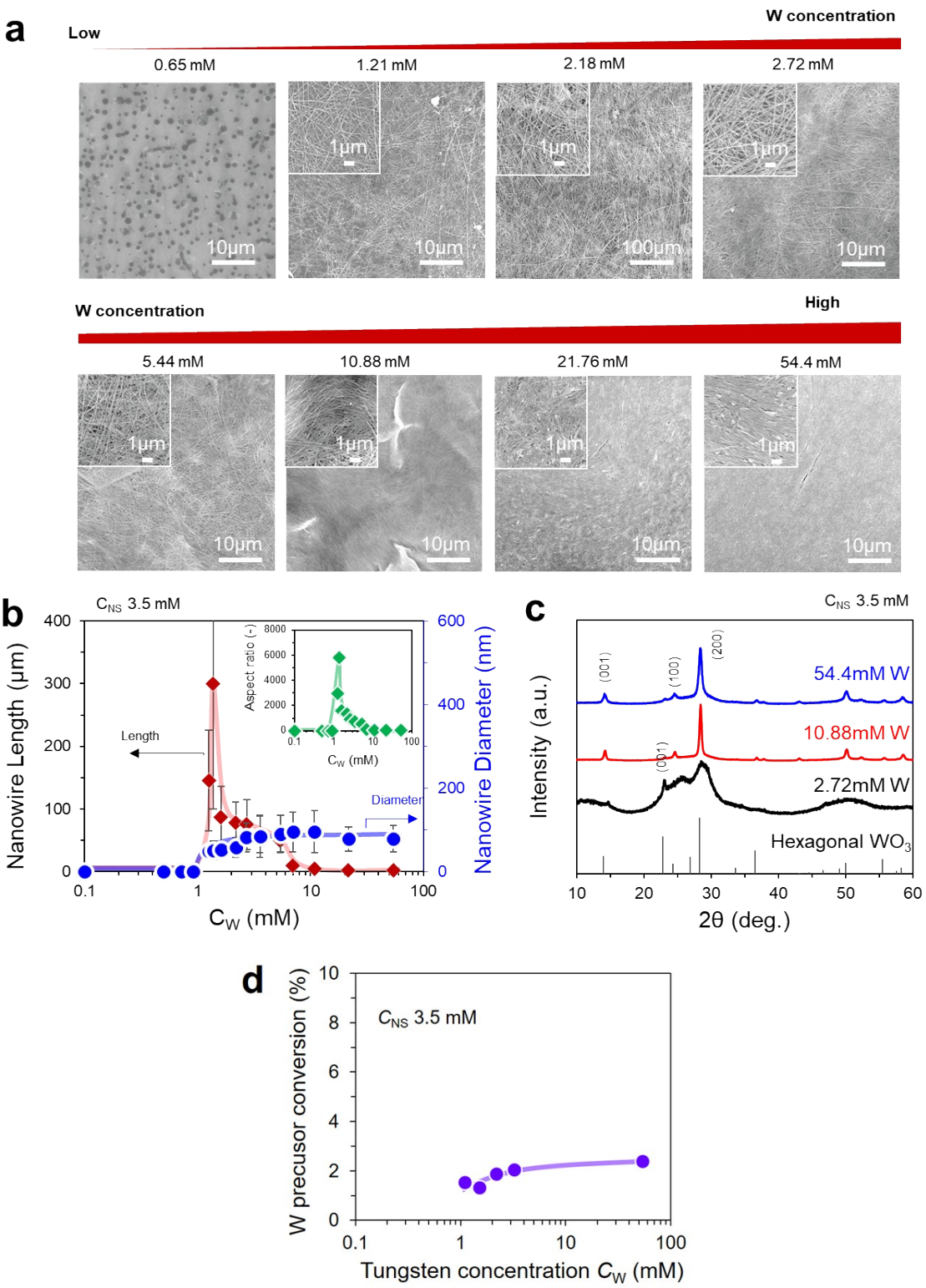

Figure S3. Effect of tungsten precursor concentration (C_W) on *h*-WO_3 nanowire morphologies (With Na_2SO_4, 3.5 mM) when varying concentration of tungstic acid sol from 0.65 to 54.4 mM. All growth experiments are performed at 200°C for 24 h, initial pH 1.68. (a) SEM images of nanowires grown with increasing of C_{NS}; (b) Tungsten precursor concentration dependence on the nanowire morphology data (including length and radius, from (a)) and the aspect ratio (insert); (c) XRD patterns of *h*-WO_3 nanowires grown with different concentration of tungsten precursor. (d) W precursor conversion ratio varied with the initial concentration.

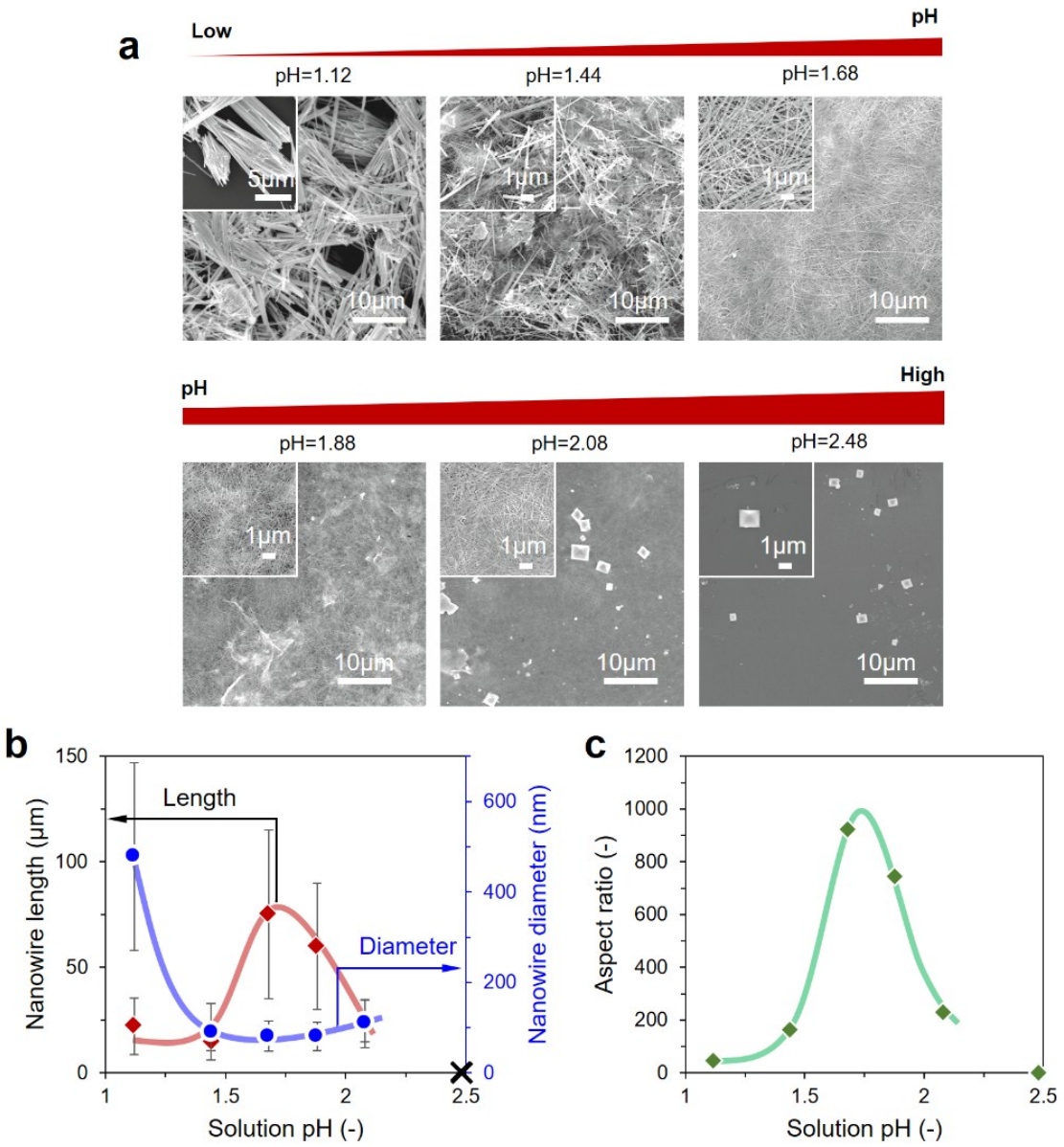

Figure S4. Effect of pH on *h*-WO_3 nanowire morphologies (2.72mM tungsten precursor, 3.5mM Na_2SO_4) when varying pH from 1.12 to 2.48. All growth experiments are performed at 200°C for 24 h. (a) SEM images of nanowires grown with different pH; (b) Solution pH dependence on the nanowire morphology data (including length and radius, from (a)); (c) Solution pH dependence on the nanowire aspect ratio (from (b)).

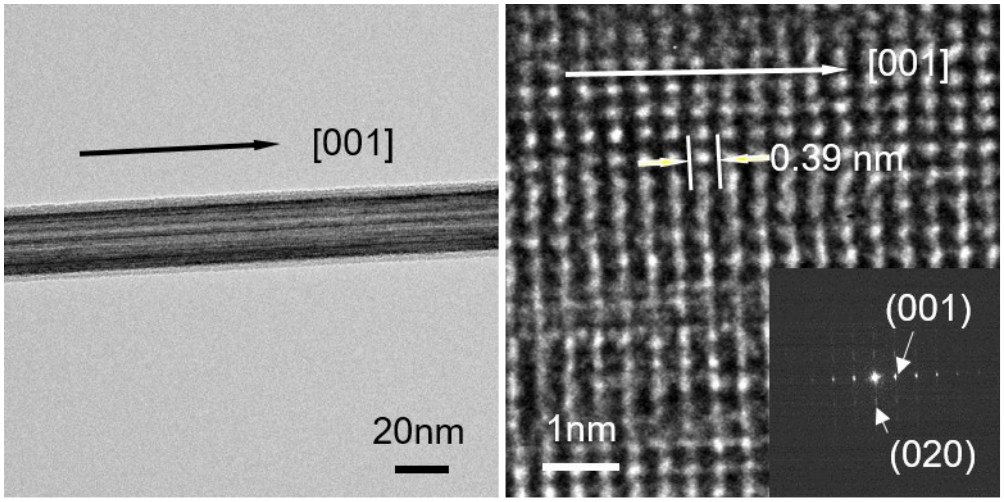

Figure S5. TEM characterizations of the as-grown WO_3 nanowire. (Growth condition, C_W, 2.72 mW, C_{NS}, 3.5 mM)

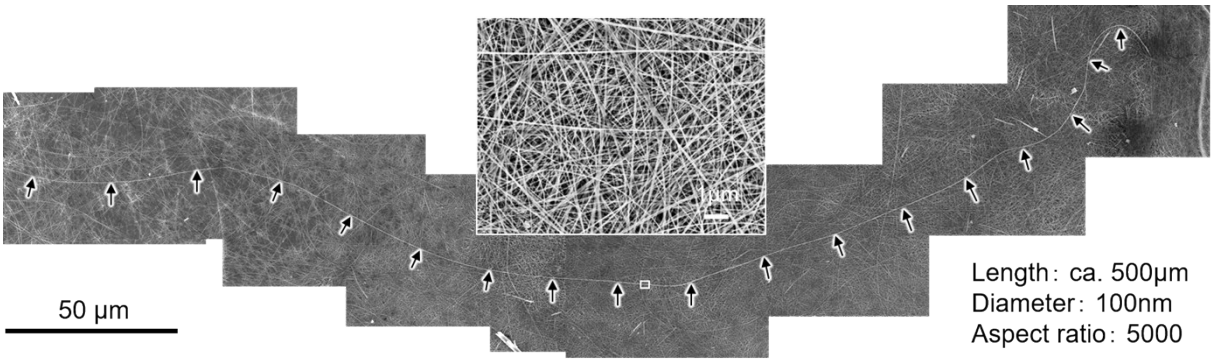

Figure S6. SEM images of single ca. 500 μm long WO_3 nanowire. (Growth condition, C_W, 1.38 mW, C_{NS}, 3.5 mM)

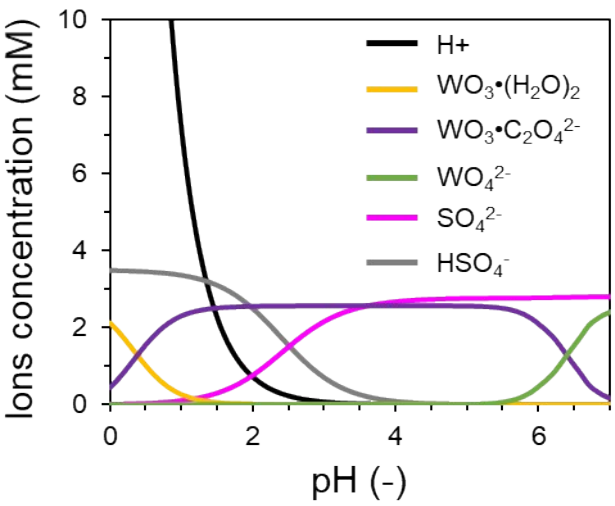

Figure S7. Calculated data of pH dependent equilibrium concentrations of ionic species in the growth solutions with 2.72mM tungsten precursor and 3.5mM Na_2SO_4.

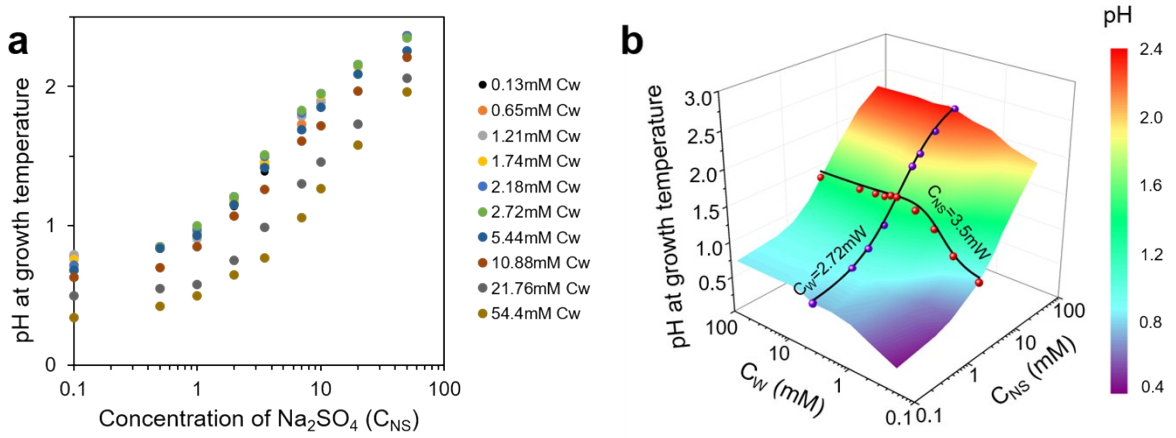

Figure S8. pH of the growth solution after addition of different concentration of Na_2SO_4 at growth temperature.

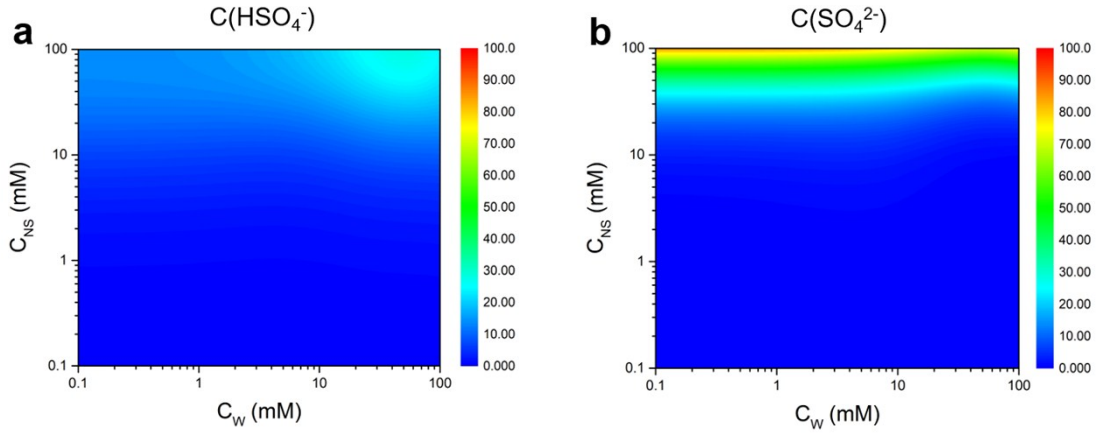

Figure S9. The calculated populations of two sulfur oxoanions (SO_4^{2-} and HSO_4^-) varied with concentration of tungsten precursor and Na_2SO_4.

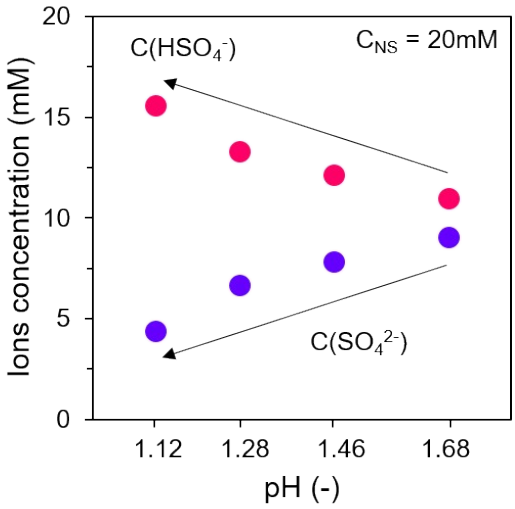

Figure S10. Calculated equilibrium ion concentrations of HSO_4^- and SO_4^{2-} for the pH ranged from 1.68 to 1.12 (C_{NS} controlled to be 20 mM).

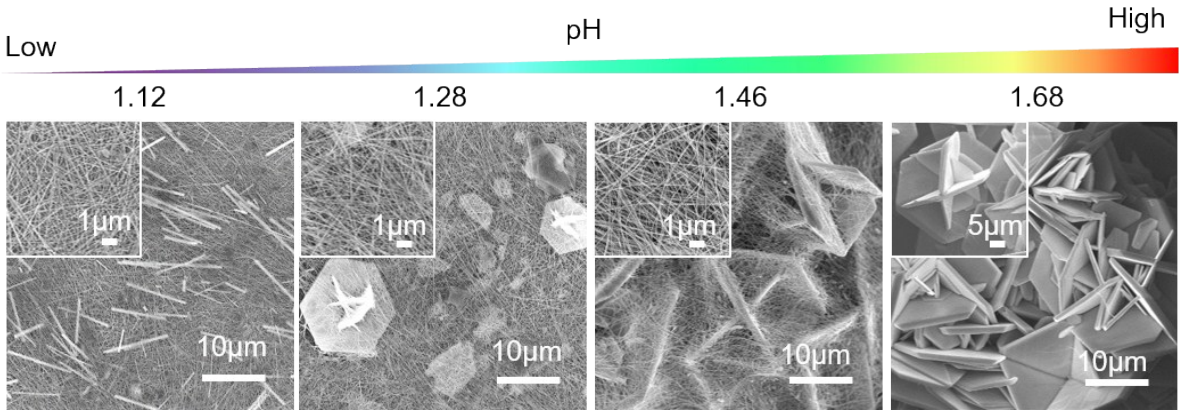

Figure S11. SEM images of fabricated WO_3 nanostructures when varying pH values ranged from 1.68 to 1.12 (C_{NS} controlled to be 20 mM).

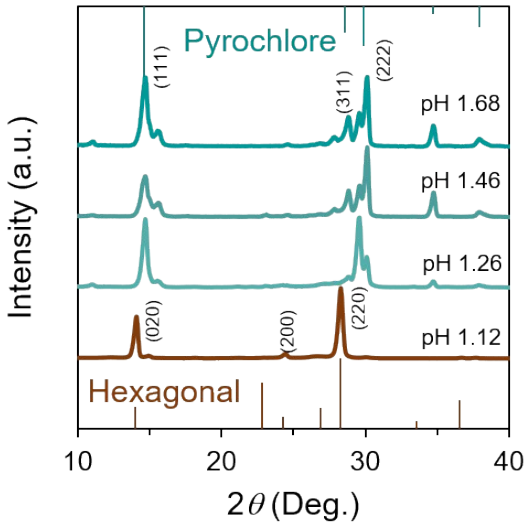

Figure S12. XRD data of the fabricated WO_3 nanostructures when varying pH values ranged from 1.68 to 1.12 (C_{NS} controlled to be 20 mM).

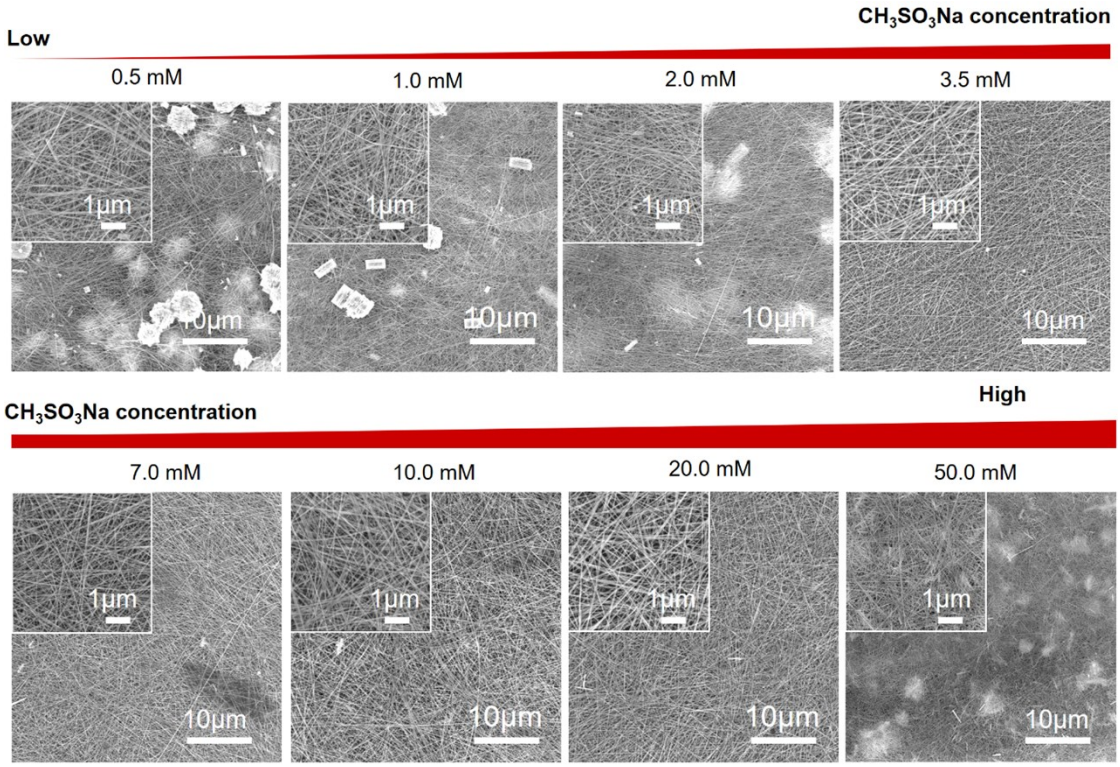

Figure S13. Effect of Na_2SO_4 concentration (C_{NS}) on *h*-WO_3 nanowire morphologies (2.72mM tungsten precursor) when varying concentration of Na_2SO_4 from 0.5 to 50mM. All growth experiments are performed at 200°C for 24 h, initial pH 1.68.

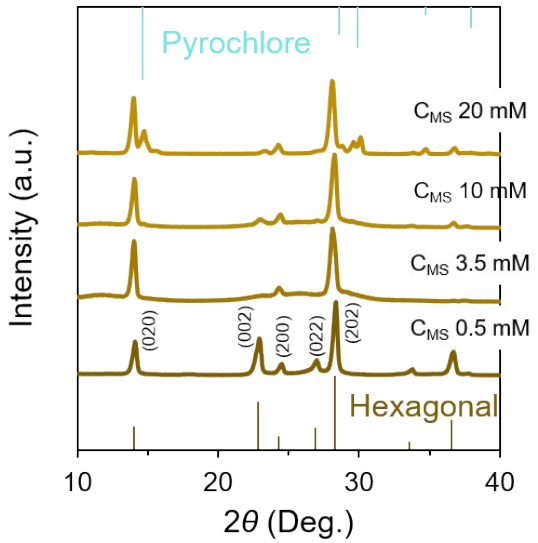

Figure S14. XRD data of the fabricated WO_3 nanostructures when varying concentration of CH_3SO_3Na (C_W controlled to be 2.72 mM).

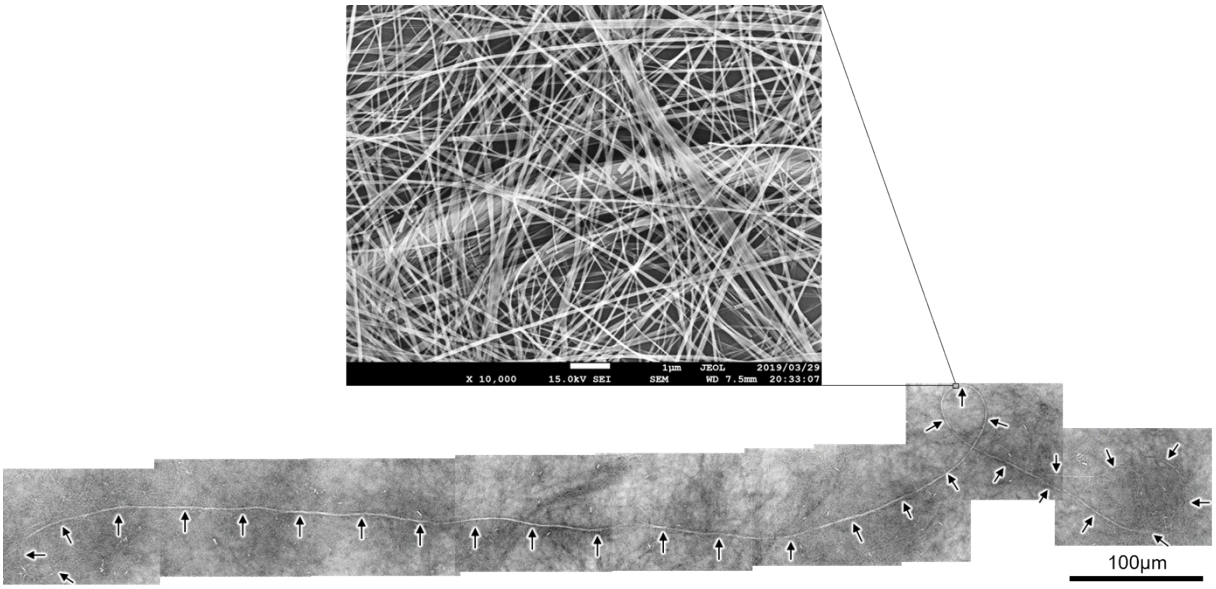

Figure S15. Millimeter-long *h*-WO_3 nanowire when controlling C_W (2.18mM) and C_{MS} (6mM).

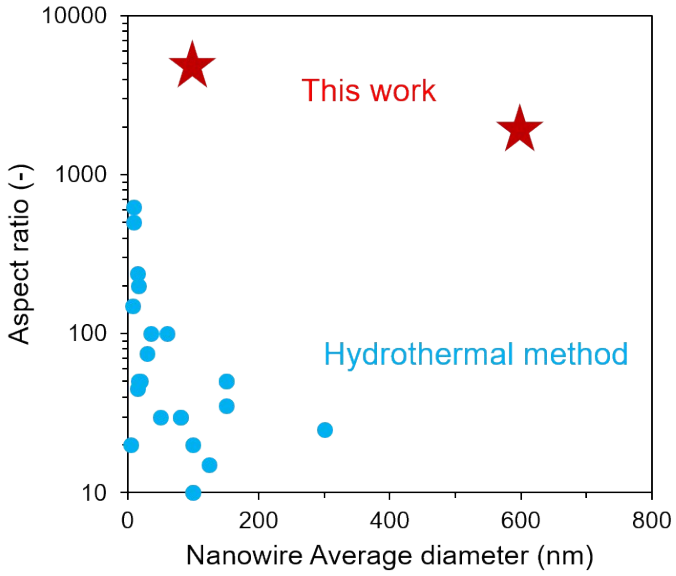

Figure S16. Comparison between the WO_3 nanowires obtained in this work and previous works on the aspect ratio.

Table S1. Comparison of one-dimensional tungsten oxide nanowire grown by hydrothermal method.

Tungsten oxide nanowires	Capping agent	Nanowire diameter/Nanowire length	Reference
Hexagonal WO_3 nanowire	**Na_2SO_4/CH_3SO_3Na**	**20-1000nm/ hundreds of micrometers~1.2 Millimeters**	**This work**
	Li_2SO_4/Na_2SO_4/K_2SO_4/ Rb_2SO_4/$(NH_4)_2SO_4$	5-1000nm/ hundreds of nanometers ~tens of micrometers	[2]
	NaCl	20~100nm/2 μm	[3]
	$C_nH_{(2n+1)}SO_4Na$ (n=10, 12,14)	50nm/1.5-5 μm	[4]
	$SnCl_4 \cdot 5H_2O$	300nm/5 μm	[5]
Monoclinic $W_{18}O_{49}$ nanowire	Na_2SO_4/$(NH_4)_2SO_4$	3-1000nm/ hundreds of nanometers ~tens of micrometers	[2(a)], [6]
	Cetyltrimethylammonium bromide (CTAB)	17nm/several micrometers	[2(b)]
	p-aminobenzoic acid (PABA)	5nm/ hundreds of nanometers	[7-8]
	PVP	5nm/tens of micrometers	[9]

Part II Computational Details

We used density functional theory (DFT) to compute adsorption energies of SO_4^{2-} and HSO_4^- on the *h*-WO_3 (001) and (100) planes. Different levels of theory were combined via the ONIOM extrapolation scheme, which allowed both to consider hydration effects and to refine results from pure DFT by exact-exchange hybrid DFT calculations. In this study, the ONIOM energy E_{ONIOM} was defined as $E_{ONIOM} = E_{periodic}^{Low} - E_{finite}^{Low} + E_{finite}^{High}$. $E_{periodic}^{Low}$ indicates low-level DFT energy of a periodic slab model, while E_{finite}^{Low} means the energy of a finite-size fragment of the slab model computed at the same level of theory. E_{finite}^{High} is high-level DFT energy of the fragment with an implicit solvent model. The slab model for the *h*-WO_3 (100) surface consisted of (2×2)-supercell (*a*=15.0Å, *b*=7.7Å) with 13 atomic layers and the 20Å vacuum region, while the (001) slab model consisted of (2×2)-supercell (*a*=*b*=15.0Å) with 5 atomic layers. The finite-size fragment used to compute E_{finite}^{Low} and E_{finite}^{High} consisted of adsorbate, a fragment of the surface at the adsorption site W_2O_9, and link hydrogen atoms. The link atoms were placed along each W-O bond on the boundary between the fragment and non-fragment regions. The bond length between a boundary oxygen atom and a link atom was set to be 1.0Å. Moreover, one or two protons were introduced on the surface to maintain cell's charge neutrality.

All the low-level DFT calculations were carried out with Vienna Ab initio Simulation Package (VASP) version 5.4.4.[10-13] RPBE was chosen for the exchange-correlation functional. Core-electrons were treated by the projector-augmented wave (PAW) approach. We adopted the gamma point approximation and the Gaussian smearing method with a width of 0.05 eV. The cut-off energies were 400eV for geometry optimizations and 520eV adsorption energy calculations, respectively. The convergence criterion for geometry optimizations was set to be 0.01eV/Å. High-level DFT calculations were performed at the B3LYP/def2-TZVPP level of theory using Gaussian 16 program package Revision A. 03.

They incorporated hydration effects by the SMD implicit solvation method developed by Truhlar and his coworkers.[14] Adsorption energy was evaluated by the energy difference between the adsorbed and desorbed states. The initial geometry of the desorbed state was prepared by lifting the adsorbed molecule along the surface normal by 5Å. The geometry of the desorbed slab model was optimized using low-level DFT while fixing the position of sulfur.

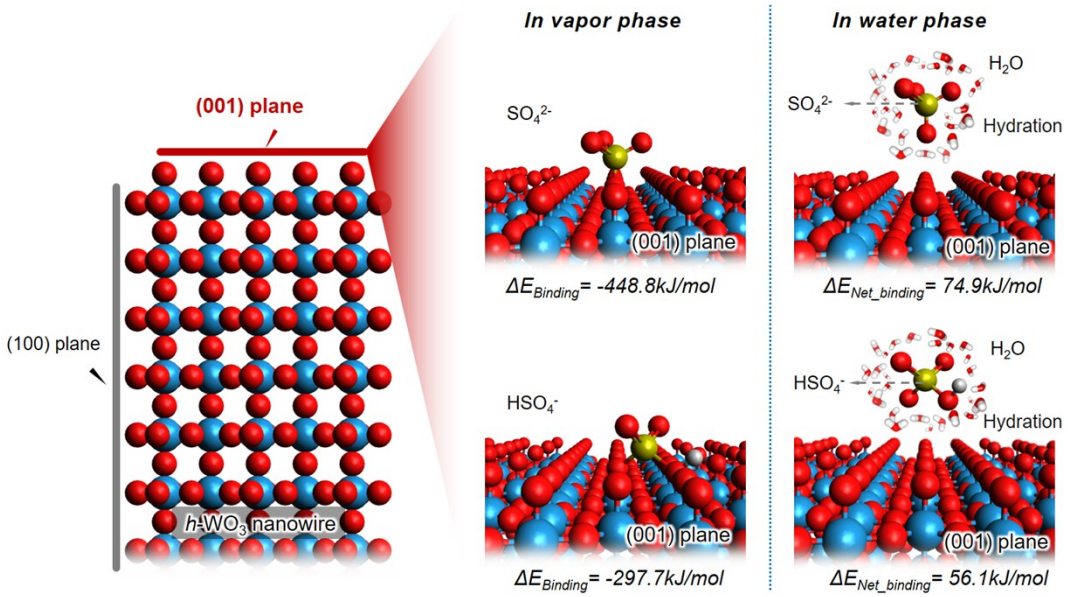

Figure S17. Calculated binding energy of both sulfur oxoanions (HSO_4^- and SO_4^{2-}) on the plane (001) of hexagonal WO_3 in vapour and water phase. The coordination structures are simulated by DFT calculation.

Part III Nonanal sensing properties of the *h*-WO_3 nanowire based flexible sensor devices

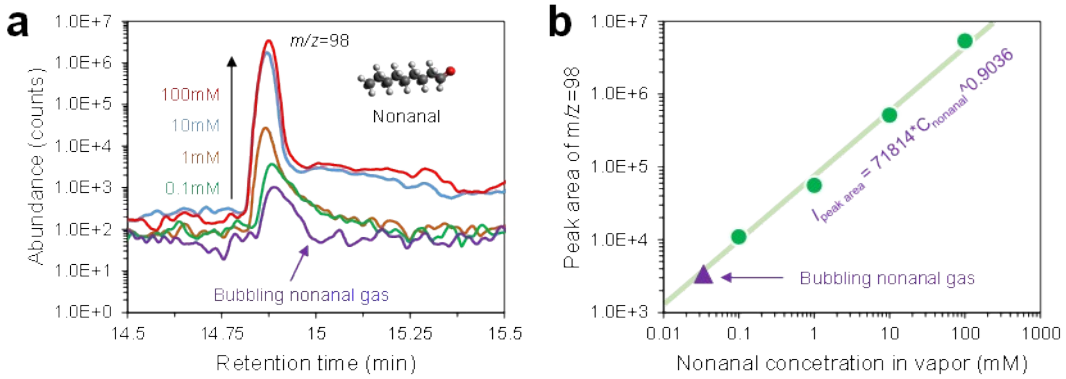

Figure S18. Nonanal concentration calibration by gas chromatograph mass spectroscopy (GC-MS).

For the bubbling nonanal gas, the detailed calibration method is presented as follows. Firstly, different mole ratio of nonanal and isopropanol solutions (1-nonanal/isopropanol = 0.1/1, 1/1, 10/ 1 and 100/1, mM/M) were distributed. Then 10 μL of the mixed solution was injected into the heating chamber of the GC-MS. After the evaporation of the liquid solution, the vapor gas was blown into the chromatographic column by Ar and detected by the mass spectroscopy. Figure S18a shows the GCMS spectra for nonanal measured at *m*/*z*=98 with different mole ratio. Here, the integral area of the peak can be utilized to calculate the concentration of the nonanal. Figure S18b plotted the integral area of the peak at *m*/*z*=98 that varied with the nonanal concentration. According to the obtained calibration curve, the concentration of the nonanal bubbling gas can be quantitatively measured. To reduce the test error, each mole ratio of nonanal tested for 3 times.

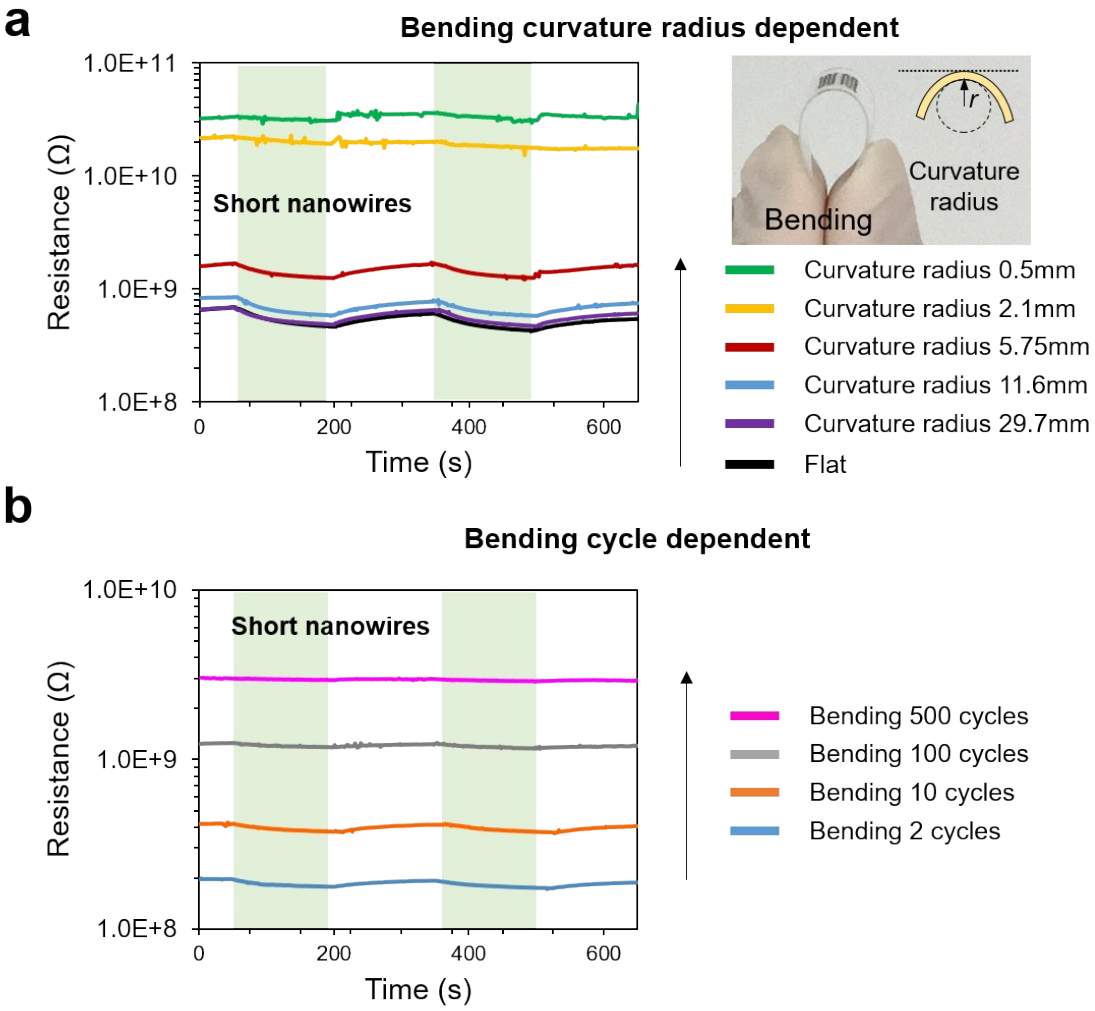

Figure S19. Dynamic resistance curves of the **Short** WO_3 nanowire device to 2.62 ppm nonanal with different bending curvature radius and bending cycles. (a) Bending curvature radius dependent gas sensing performance and (b) bending cycles dependent gas sensing performance.

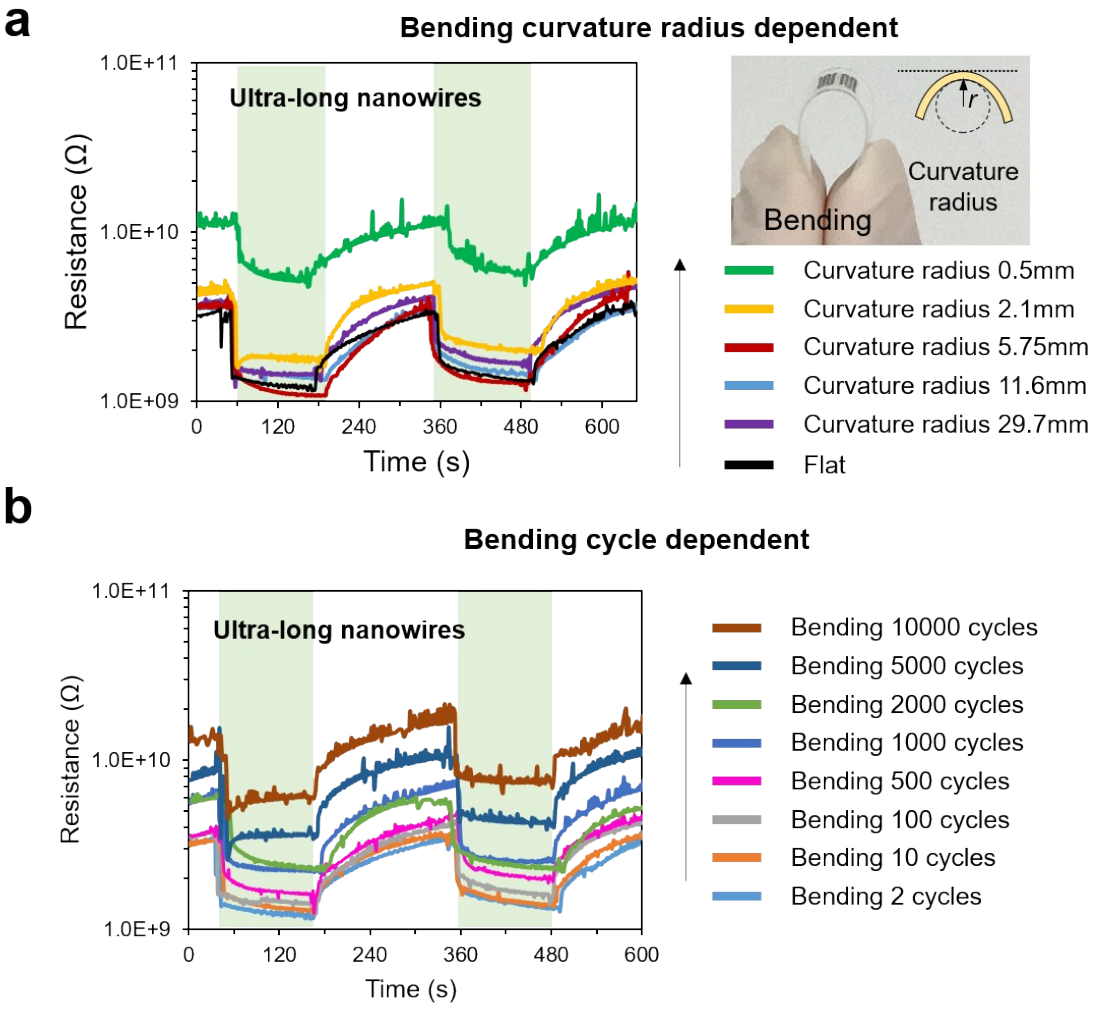

Figure S20. Dynamic resistance curves of the **Ultra-long** WO_3 nanowire device to 2.62 ppm nonanal with different bending curvature radius and bending cycles. (a) Bending curvature radius dependent gas sensing performance and (b) bending cycles dependent gas sensing performance.

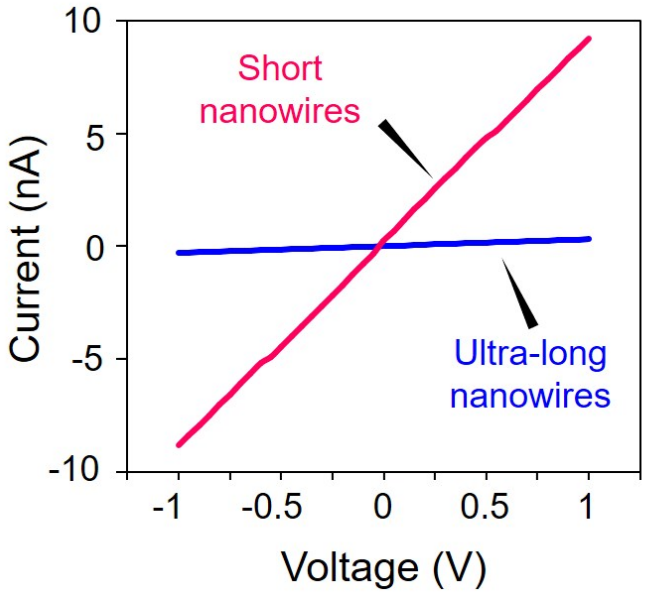

Figure S21. *I-V* characteristics of the ultra-long and short nanowire film devices. Measure at room temperature and atmosphere pressure.

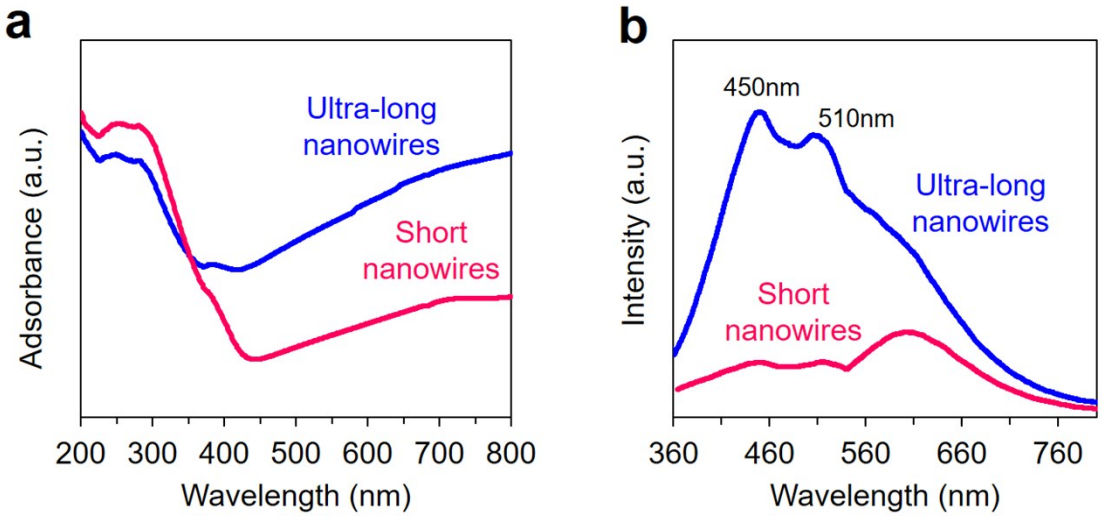

Figure S22. (**a**) Ultraviolet–visible absorption spectra data and (**b**) photoluminescence spectra data of the as-grown ultra-long and short *h*-WO_3 nanowires.

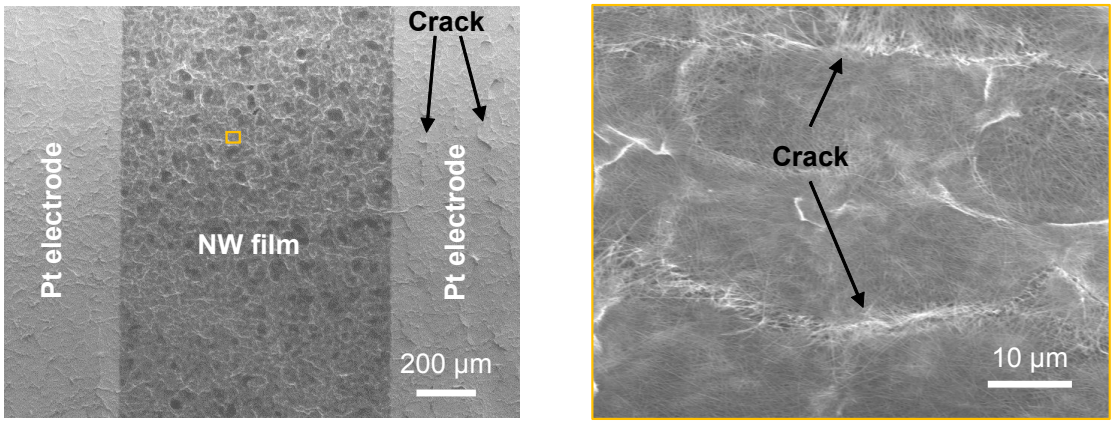

Figure S23. SEM images of the flexible ultra-long nanowire based sensor device after bending with 10000 cycles.

References

[1] Lee, T.; Lee, Y.; Jang, W.; Soon, A. *J. Mater. Chem. A* **2016**, 4, 11498.

[2] (a) Gu, Z.; Ma, Y.; Yang, W. *Chem. Commun.* **2005**, 0, 3597. (b) Gu, Z.; Zhai, T.; Gao, B.; Sheng, X.; Wang, Y.; Fu, H.; Ma, Y.; Yao, J. *J. Phys. Chem. B* **2006**, 110, 23829. (c) Gu, Z.; Li, H.; Zhai, T.; Yang, W.; Xia, Y.; Ma, Y.; Yao, J. *J. Solid State Chem.* **2007**, 180, 98. (d) Song, X. C.; Zheng, Y. F.; Yang, E.; Wang, Y. *Mater. Lett.* **2007**, 61, 3904. (e) Huang, K.; Pan, Q.; Yang, F.; Ni, S.; Wei, X.; He, D. *J. Phys. D-Appl. Phys.* **2008**, 41, 155417. (f) Phuruangrat, A.; Ham, D. J.; Hong, S. J.; Thongtem, S.; Lee, J. S. *J. Mater. Chem.* **2010**, 20, 1683. (g) Zhang, J.; Tu, J. P.; Xia, X. H.; Wang, X. L.; Gu, C. D. *J. Mater. Chem.* **2011**, 21, 5492. (h) Shi, J.; Hu, G.; Cong, R.; Bu, H.; Dai, N. *New J. Chem.* 2013, 37, 1538. (i) Ha, J. H.; Muralidharan, P.; Kim, D. K. *J. Alloys Compd.* **2009**, 475, 446. (j) Huang, K.; Zhang, Q.; Yang, F.; He, D. *Nano Res.* **2010**, 3, 281. (k) Gao, L.; Wang, X.; Xie, Z.; Song, W.; Wang, L.; Wu, X.; Qu, F.; Chen, D.; Shen, G. *J. Mater. Chem. A* **2013**, 1, 7167. (l) Zeng, W.; Miao, B.; Li, T.; Zhang, H.; Hussain, S.; Li, Y.; Yu, W. *Thin Solid Films* **2015**, 584, 294. (m) Cai, Z. X.; Li, H. Y.; Yang, X. N.; Guo, X. *Sens. Actuators, B* **2015**, *219*, 346. (n) Miao, B.; Zeng, W.; Hussain, S.; Mei, Q.; Xu, S.; Zhang, H.; Li, Y.; Li, T.; *Mater. Lett.* **2015**, 147, 12. (o) Zhou, Y,; Peng, Y. H.; Yin, Y. L.; Zhou, F.; Liu, C.; Ling, J.; Lei, L.; Zhou, W. C.; Tang, D. S. *Sci. Rep.* **2016**, 6, 32712. (p) Nagy, D.; Firkala, T.; Drotár, E.; Szegedi, Á.; László, K.; Szilágyi I.M. *RSC Adv.* **2016**, 6, 95369. (q) Yao, S.; Qu, F.; Wang, G.; Wu, X. *J. Alloys Compd.* **2017**, *724*, 695.

[3] (a) Wang, J.; Khoo, E.; Lee, P. S.; Ma, J. *J. Phys. Chem. C* **2008**, 112, 14306. (b) Wang, J.; Khoo, E.; Lee, P. S.; Ma, J. *J. Phys. Chem. C* **2009**, 113, 9655.

[4] Salmaoui, S.; Sediri, F.; Gharbi, N.; Perruchot, C.; Jouini, M. *Electrochim. Acta* **2013**, 108, 634.

[5] Hu, P.F.; Chen, Y.; Chen, Y.; Lin, Z.H.; Wang, Z.C. *Physica E* **2017**, 92, 12.

[6] Zhang, J.; Zhang, H.; Liu, L.; Li, F.; Wang S. *Chem. Phys. Lett.* ***2018,*** 706, 243.

[7] Gao, X. Q.; Xiao, F.; Yang, C.; Wang, J. D.; Su, X. T. *J. Mater. Chem. A* **2013**, 1, 5831.

[8] Hang, C.; Cai, W.; Gao, X.; Luo, J.; Su, X. *Adv. Powder Technol.* **2018**, *29*, 1272.

[9] Liu, J. W.; Zheng, J.; Wang, J. L.; Xu, J.; Li, H. H.; Yu, S. H. *Nano Lett.* **2013**, 13, 3589.

[10] Kresse, G.; Hafner, J. *Phys. Rev. B* 47, **1993**, 558.

[11] Kresse, G,; Hafner, J. *Phys. Rev. B* 49, **1994**, 14251.

[12] Kresse, G.; Furthmüller, J. *Comput. Mater. Sci.* 6, **1996**, 15.
[13] Kresse, G.; Furthmüller, J. *Phys. Rev. B* 54, **1996**, 11169.
[14] Marenich, A. V.; Cramer, C. J.; Truhlar, D. G. *J. Phys. Chem. B* 113, **2009**, 6378.